journal

J. Am. Ceram. Soc., 99 [11] 3610–3615 (2016)
DOI: 10.1111/jace.14374

Lattice Dynamics, Dielectric Constants, and Phase Diagram of Bismuth Layered Ferroelectric $Bi_3Ti_{1-x}W_xNbO_{9+\delta}$ Ceramics

Jinzhong Zhang,[‡] Kai Jiang,[‡] Zhiyong Zhou,[§] Zhigao Hu,[‡,†] Genshui Wang,[§] Xianlin Dong,[§] and Junhao Chu[‡]

[‡]Department of Electronic Engineering, East China Normal University, Shanghai 200241, China

[§]Key Laboratory of Inorganic Functional Material and Device, Shanghai Institute of Ceramics, Chinese Academy of Sciences, Shanghai 201800, China

Lattice dynamics and phase transitions of Aurivillius ferroelectric $Bi_3Ti_{1-x}W_xNbO_{9+\delta}$ (BTWN100x, $0 \le x \le 15\%$) ceramics have been investigated by temperature-dependent Raman spectra (80–800 K) and far-infrared (FIR) reflectance spectra (6–300 K). The frequency, intensity, and line width of phonon modes as well as complex dielectric functions of BTWN100x ceramics have been extracted by fitting Raman and FIR reflectance spectra with the multi-Lorentzian oscillator model. It was found that the dielectric constants at a certain frequency region become lower with increasing W compositions at room temperature due to the compressive stress on W–O bands. Moreover, the temperature-dependent behavior of optical phonon modes in BTWN100x ceramics indicates that there are two intermediate phases during the phase transition from paraelectric *I4/mmm* to ferroelectric $A2_1am$ phase on cooling. The phase diagram of BTWN100x ceramics as a function of W composition has been improved.

Keywords: *Aurivillius compounds; compositional effects; Raman and infrared spectra; phonon modes; phase diagram*

I. Introduction

Bismuth layer structured ferroelectrics have potential applications in nonvolatile ferroelectric random access memories and high-temperature piezoelectric device. Especially, Bi_3TiNbO_9 (BTNO) has attracted much attention because of its high Curie temperature (T_C ~1213 K), lead free, and excellent fatigue endurance properties.[1–4] The crystal structure of BTNO could be described as alternate layers of $(Bi_2O_2)^{2+}$ slabs and two perovskite-type $(BiTiNbO_7)^{2-}$ blocks along orthorhombic c-axis direction.[5] The microstructure and electrical properties of BTNO and its intergrowth compounds (Bi_2WO_6–Bi_3TiNbO_9, $SrBi_2Ta_2O_6$–Bi_3TiNbO_9, etc.) have been reported.[5–8] BTNO is described as a tetragonal prototype (*I4/mmm*) at high temperature above Curie temperature, although it is difficult to identify its ferroelectric phase from symmetries *Fmmm, Amam*, *F2mm*, *Abam*, $A2_1am$, etc due to its complicated structure below T_C. Thompson et al. pointed out that its structure belongs to orthorhombic $A2_1am$ symmetry detected by convergent-beam electron diffraction patterns,[5] whereas Zhang et al. argued that its lattice parameters obtained by (XRD) patterns are close to those of *Fmmm* symmetry at room temperature.[8] Moreover, its saturation polarization P_s value can be about 27.7 μC/cm^2 from the theoretical calculations.[8] Irie et al. found that the ferroelectric spontaneous polarization of displacive ferroelectrics $(Bi_2O_2)(A_{n-1}B_nO_{3n+1})$ ($n = 2$ for BTNO) originates from the BO_6 octahedra in the perovskite block, and spontaneous polarization occurs mainly in the direction parallel to the bismuth layer.[9] However, the piezoactivity of pure BTNO ceramics is very low ($d_{33} < 7$ pC/N) and has a relatively low resistivity for applications.[10]

Element doping can affect octahedral distortion and thus tune physical properties such as Curie temperature, ferroelectric, and dielectric properties.[11–16] In BTNO, Bi^{3+} vacancies will be created and it causes formation of oxygen vacancies in both perovskite and $(Bi_2O_2)^{2+}$ layers due to bismuth evaporation during annealing in sample preparation process.[6] Electrons released from oxygen vacancies can occupy 3*d* states. Thus, reducing occupations of 3*d* states by electrons should be important to improve electric properties by means of element doping. According to previous investigation, these dopants should satisfy two major circumstances:[15] firstly, their valence states should be higher than that of Ti^{4+} ions; secondly, they should be in concert with the original B-site Ti^{4+} ions in radii. Zhou et al. reported that W^{6+} is placed into the octahedra and possibly occupy Ti^{4+} sites based on XRD analysis, and Bi–W–O block should be much firmer than Bi–Ti–O block with respect to the metallicity of W^{6+} ions. The W^{6+} cations decrease oxygen vacancies and make the polar ions more movable, which effectively improve ferroelectric fatigue. In addition, the Curie temperature of $Bi_3Ti_{1-x}W_xNbO_{9+\delta}$ ($0\% \le x \le 15\%$) ceramics decreases with increasing amount of W doping, which has been studied by temperature-dependent dielectric constant measured at 1 MHz above room temperature.[15] However, the doping effects on structure distortion and physical properties of BTNO ceramics have not been understood well. Vibrational studies can give the information about the structure distortion, which is related to displacements of atoms or ions.[16–18] Therefore, the effects of W doping on BTNO ceramics can be investigated by Raman and far-infrared (FIR) spectra as direct electrical capacitance measurements of the ferroelectric order are often complicated and hindered by parasitic charges forming at interface and electrodes.[4,19]

In this article, optical phonon modes of the $Bi_3Ti_{1-x}W_xNbO_{9+\delta}$ ($0\% \le x \le 15\%$) ceramics have been investigated in detail by studying temperature-dependent Raman spectra and FIR reflectance spectra. Two intermediate phase transitions are extracted based on the various temperature-dependent trends of Raman- and infrared-active modes in the temperature region of 6–800 K.

II. Experimental Procedure

Polycrystalline ferroelectric $Bi_3Ti_{1-x}W_xNbO_{9+\delta}$ (BTWN100x, x = 0%, 1%, 2%, 3%, 5%, 10%, and 15% abbreviated as BTNO, BTWN1, BTWN2, BTWN3, BTWN5, BTWN10, and BTWN15) ceramics were prepared by solid-state reaction sintering according to the scheme: $3Bi_2O_3 + 2(1-x)TiO_2 + 2xWO_3 + Nb_2O_5 \rightarrow 2Bi_3Ti_{1-x}W_xNbO_{9+x}$. The starting raw

P. Davies—contributing editor

Manuscript No. 38393. Received March 30, 2016; approved June 9, 2016.
[†]Author to whom correspondence should be addressed. e-mail: zghu@ee.ecnu.edu.cn

materials Bi_2O_3 (99.95%), TiO_2 (98.92%), Nb_2O_5 (99.95%), and WO_3 (99.00%) were mixed by ball milling in ethanol for 24 h. The mixtures with different WO_3 concentration were dried and sieved to below 250 μm, and then calcined at 900°C for 2 h. The powders were finally pressed into disks of 15 mm diameter and 2 mm thickness in a steel die at a pressure of about 200 MPa. Then they were heated to about 800°C to remove binder. Finally, the disk-shaped samples were placed in a sealed Al_2O_3 crucible and sintered for 1 h at 1120°C–1150°C in air. Detailed preparation process could be found elsewhere.[15]

The crystalline structure of BTWN100x ceramics was investigated by XRD using a Ni filtered CuK_α radiation source (D/MAX-2550V; Rigaku Co., Akishima-shi, Tokyo, Japan). In the XRD measurement a vertical goniometer (Model RINT2000; Rigaku Co) was used, and continuous scanning mode (θ–2θ) was selected with a scanning rate of 10°/min and interval of 0.02°. Temperature-dependent Raman spectra were collected by using a micro-Raman spectrometer with a spectral resolution of 1 cm^{-1} (Jobin-Yvon LabRAM HR 800 UV, Longjumeau, Paris, France) in the temperature range 80–800 K with a precision of about 0.5 K. The He–Ne laser with the wavelength of 632.8 nm was taken as the exciting source. The laser beam was focused through a 50× microscope with a working distance of 18 mm. An air cooled charge coupled device (−70°C) with a 1024 pixels × 256 pixels front illuminated chip was used to collect the scattered signal dispersed on 1800 grooves/mm grating. Note that all measured Raman spectra have been divided by the Bose-Einstein occupation number $n(\omega)+1 = 1/[1-\exp(-\hbar\omega/k_BT)]$ ($\hbar$ and k_B are Planck constant and Boltzmann constant, respectively) to get rid of the trivial temperature dependence.[20] FIR reflectance spectra of the BTWN100x ceramics were measured by Bruker Vertex 80V Fourier transform infrared spectrometer (Bruker Co., Billerica, MA) equipped with a 6-μm-thick mylar beam splitter, a DTGS detector, and a Hg lamp source. The externally incident angle is set as 6°. The samples are fixed into an Oxford Optistat AC-V12w Continuous-flow cryostat in He vapor (Oxford Instruments PLC, Abingdon, Oxfordshire, England). Gold mirror, whose absolute reflectance amplitude is recorded, is adopted as a reference for the FIR spectra.

III. Results and Discussion

The XRD patterns of W-doping BTNO ceramics measured at room temperature reveal an orthorhombic phase within the W composition below 15%, as shown in Fig. 1. The strongest diffraction near 29.4° is assigned to (115) peak, which is consistent with the strongest diffraction peak ($11\underline{2}n+1$) from Aurivillius phase.[15] Moreover, there are some other diffraction peaks such as (113), (008), (020)/(200), (00$\underline{1}$0), (220), (20$\underline{1}$0)/(02$\underline{1}$0), (131)/(311), and (135)/(315), and secondary phases are not observed, which suggests that W^{6+} ions are incorporated into the BTNO matrix and presumably occupied Ti^{4+} sites. According to the positions of (115), (020)/(200), and (220) diffraction peaks, their lattice constants have the similar values of about $a \approx b = 5.434$ Å and $c = 25.18$ Å, which are close to those of the orthorhombic $A2_1am$ (36) phase of BTNO (JCPDF No. 79-1550, Cell = 5.44 Å × 5.39 Å × 25.10 Å⟨90 × 90 × 90⟩).

As an approximation, it is helpful to assign tetragonal symmetry ($I4/mmm$, D_{4h}^{17}) to BTNO at the temperature above T_C. Accordingly, one may generate Raman- and infrared (IR)-active modes at $q = 0$ for the paraelectric phase: $4A_{1g}(R) + 2B_{1g}(R) + 6E_g(R) + 6A_{2u}(IR) + B_{2u}(S) + 7E_u(IR)$, where R, IR, and S stand for Raman-active, infrared-active, and silent modes, respectively. Accurately, A_{1g}, B_{1g}, and E_g are Raman active in (xx, yy, zz), (xx, yy), and (xy, yz) scattering geometries, respectively. Moreover, the modes A_{2u} and E_u are infrared active for z and xy light polarizations, respectively.[21] On the other hand, the orthorhombic parent structure $Fmmm$ is predicted to have 24 first-order Raman-active modes ($6A_g + 2B_{1g} + 8B_{2g} + 8B_{3g}$), 28 first-order IR-active modes ($8B_{1u} + 10B_{2u} + 10B_{3u}$), and 2 inactive modes ($2A_u$) at the Γ point of Brillouin zone.[22] Specifically, for the orthorhombic phase ($A2_1am$, C_{2v}^{12}), $\Gamma^{opt.} = 21A_1$ (R, IR) + $20A_2$ (R) + $19B_1$ (R, IR) + $21B_2$ (R, IR).[23]

At room temperature, Raman spectra of BTWN100x ceramics with different W compositions have similar shapes without peak appearing/vanishing [Fig. 2(a)]. There are 12 Raman peaks near 60, 185, 205, 290, 330, 450, 590, 820 cm^{-1}, and so on, which are observed in the wave number range from 20 to 900 cm^{-1} due to the overlapping of same symmetry vibrations or weak features of some vibration bands. Note that the mode assignments are still not clear for BTNO materials because of the large atom number of crystal unit cell and complicated crystal structure. Nevertheless, the Raman-active modes near 185 and 205 cm^{-1} are associated with the $a(b)$- and c-axis vibrations of the Ti/Nb ions, respectively. The band at about 590 cm^{-1} can be assigned to the opposing excursions of the external apical oxygen atoms of the TiO_6/NbO_6 octahedra.[13] Moreover, the one around 820 cm^{-1} relates to symmetric stretch of the

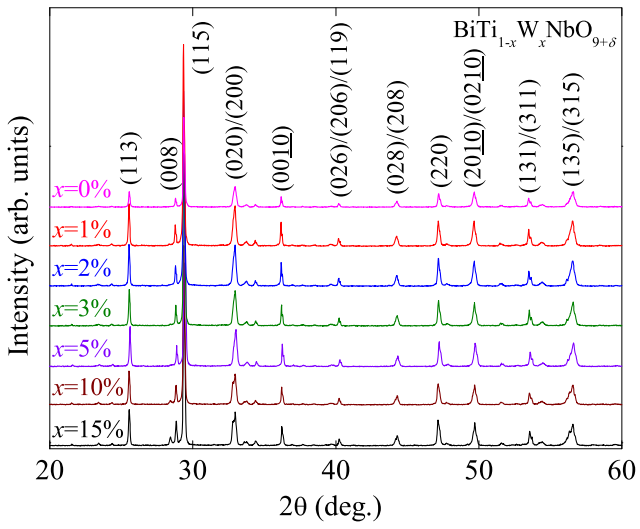

Fig. 1. The X-ray diffraction patterns of the BTWN100x ceramics with different W compositions recorded at room temperature. Note that each spectrum is shifted in intensity for clarity.

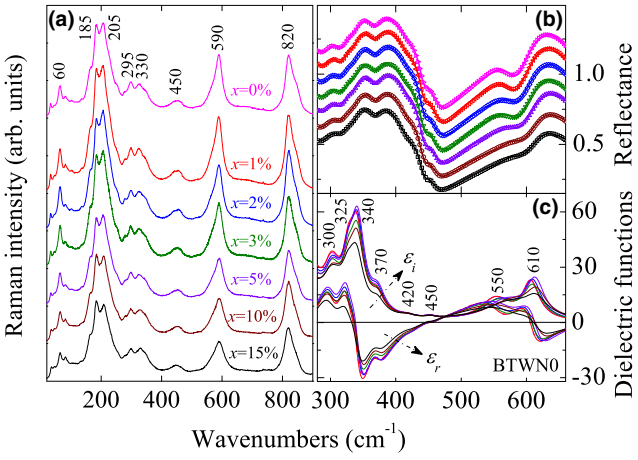

Fig. 2. (a) Raman scattering and (b) experimental (dotted lines) and best-fitted (solid lines) FIR reflectance spectra of BTWN100x ceramics with different W compositions measured at room temperature. Note that the spectra are shifted in intensity for clarity. (c) Real (ε_r) and imaginary (ε_i) parts of dielectric functions extracted by fitting FIR reflectance spectra with a multi-Lorentzian oscillator model.

Table I. The Frequencies of Some Typical Raman- and IR-Active Modes of BTWN100*x* Ceramics with Different W Compositions

W(*x*)	Raman-active modes Peak position (cm^{-1})				IR-active modes Mode frequency (cm^{-1})			
0%	183.2	205.8	589.9	820.0	326.8	340.2	549.4	605.2
1%	183.3	205.4	590.0	819.9	327.2	339.7	552.6	608.0
2%	183.2	205.7	590.6	820.3	328.4	341.2	561.8	612.5
3%	183.3	205.8	591.1	820.3	327.7	341.3	560.2	611.5
5%	183.2	206.5	591.9	820.4	328.0	341.6	569.8	615.1
10%	183.6	207.8	592.2	819.7	326.3	339.8	582.7	618.0
15%	183.7	208.6	591.7	818.4	327.3	339.9	583.1	618.2

octahedra.[24,25] In addition, the lower frequency modes below 100 cm^{-1} originate from the Bi–O bonds in $(Bi_2O_2)^{2+}$ layers against the perovskite units.[22] Peak positions of some typical Raman-active modes are listed in Table I.

Figure 2(b) presents the experimental and fitting FIR reflectance of BTWN100*x* ceramics with different W compositions measured at room temperature. They are nicely matched by a sum of independent damped harmonic oscillators in Lorentzian shapes. The complex dielectric functions can be obtained, which has the form: [18] $\tilde{\varepsilon}(\omega) = \varepsilon_r(\omega) + i\varepsilon_i(\omega) = \varepsilon_\infty + \sum_{j=1}^{n} \Delta\varepsilon\omega_j^2/(\omega_j^2 - \omega^2 - i\Gamma_j\omega)$, where ε_∞ is the high-frequency dielectric constant originating from electron transition and ω is frequency. The parameter *j* is the number of oscillators and Δε is dielectric strength contributed by the *j*th oscillator. Γ_j and ω_j are the *j*th oscillator damping and phonon frequency, respectively.[26] For the case of bulk materials, the complex dielectric function $\tilde{\varepsilon}(\omega)$ is related to the reflectance $R(\omega)$ by the relationship: [27] $R(\omega) = |\tilde{\varepsilon}(\omega)^{1/2} - 1|^2/|\tilde{\varepsilon}(\omega)^{1/2} + 1|^2$. The real $\varepsilon_r(\omega)$ and imaginary $\varepsilon_i(\omega)$ parts of dielectric functions of BTWN100*x* derived from the Lorentzian model are shown in Fig. 2(c) and the frequencies of some typical IR-active modes are listed in Table I. The dielectric functions of BTWN100*x* with different W compositions have a similar shape due to their similar FIR reflectance spectra. The distortion from the high-temperature phase prototype structure *I*4/*mmm*, which exists in all bismuth layered ceramics, is caused by compression of various displacive modes.[21] Theoretically, the modes located at about 300, 325, and 450 cm^{-1} denote $(Bi_2O_2)^{2+}$ bending motions in the direction nearly perpendicular to the layers. Moreover, the IR phonon modes around 340 and 370 cm^{-1} are assigned to the BO_6 stretching. The ones at 420, 550, and 610 cm^{-1} belong to the octahedral bending mode mainly caused by motions of equatorial oxygen atoms.[21,23] Moreover, the peak near 610 cm^{-1} has a shift toward higher wave number with increasing W composition due to the distortion in BTWN100*x* ceramics. The structural distortion induced by W^{6+} can be obtained by considering the tolerance factor $t = (R_A + R_O)/\sqrt{2}(R_B + R_O)$, where R_A, R_B, and R_O are the ionic radii of A (Bi^{3+}), B (Ti^{4+}, Nb^{5+}, and W^{6+}) cations, and O^{2-} anions, respectively. The average particle radius appropriately matches the A–O or B–O length in a cubic cell ($t = 1$). When $t < 1$, the B–O bond is longer than the A–O one. Therefore, the A–O–A structure exerts a condensation on the corner-connected octahedra, which will rotate to keep the B–O bond length.[28] In the case of W^{6+} substitution for Ti^{4+} sites, the tolerance factor of WO_6 is smaller than that of TiO_6 as W^{6+} ionic radius (0.62 Å) is slightly larger than Ti^{4+} one (0.61 Å). The compressive stress on W–O bonds in BTWN100*x* ceramics will induce lower dielectric constants.[29] Moreover, the shape of Raman and IR spectra is similar with those of some other Aurivillius compounds such as $CaBi_2Nb_2O_9$, $SrBi_2Ta_2O_9$, and $SrBi_2Nb_2O_9$, which have the similar ferroelectric orthorhombic phase ($A2_1am$) with the polarization along *a*-axis.[3,23,24,30]

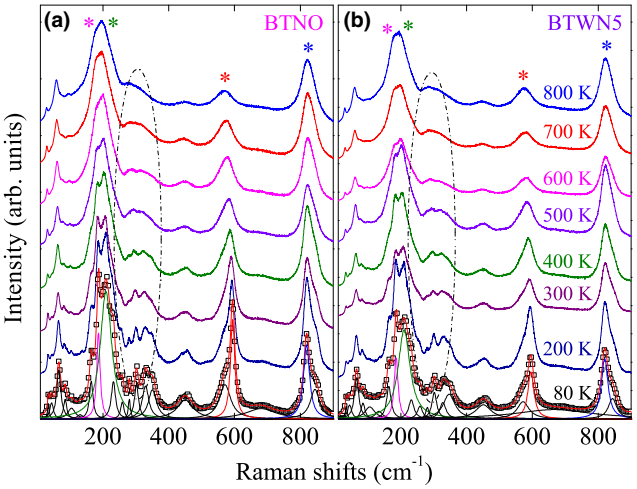

Fig. 3. Raman spectra of (a) BTNO and (b) BTWN5 ceramics at different temperature after correcting for thermal population factor and the corresponding multi-Lorentz peak fitting at 80 K. For clarity, each spectrum is shifted in intensity.

Figures 3(a) and (b) show the Raman spectra of BTN and BTWN5 ceramics recorded in the temperature range 80–800 K, respectively. At low temperature, the weak Raman peaks/shoulders cannot be assigned as they come from the first- or second-order Raman scattering and complicated unsymmetric structure. As the temperature increases, some weak modes vanished especially in the wave number range 250–350 cm^{-1}, which indicates that its crystal structure changes and the structural symmetry is improved. This phenomenon was also observed in another Aurivillius compound $SrBi_2Ta_2O_9$ and it highlights the subtle change upon heating from the ferroelectric $A2_1am$ phase to an intermediate symmetry as the number of Raman modes becomes less and less.[30] Moreover, the E_g modes of the tetragonal symmetry in the wave number range 250–350 cm^{-1} will split to lower symmetry modes (*A* and *B*) in the space group $A2_1am$ with decreasing temperature, which have been ascribed to O–Nb/Ti–O bending. To extract peak positions, intensity, and line width of the Raman phonon modes, all the Raman spectra with different temperatures and W compositions were decomposed into a series of bands with the multi-Lorentzian oscillator approximation. For example, the decomposed Raman spectra (dotted lines) of BTNO and BTWN5 ceramics at 80 K are shown in Figs. 3(a) and (b), respectively. The fitting spectra (solid lines) are in good agreement with the experimental ones. Temperature-dependent behavior of the typical modes labeled by the asterisk (*) will be discussed in the following section.

The temperature-dependent Raman modes of BTNO and BTWN5 ceramics are shown in Figs. 4(a) and (b), respectively. As mentioned above, the modes near 185 and 205 cm^{-1} are associated with the *a*(*b*)- and *c*-axis

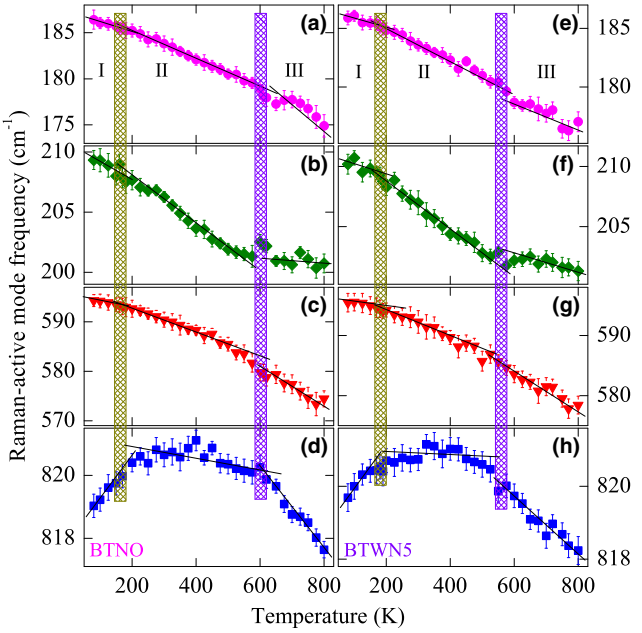

Fig. 4. The various frequency trends of some typical Raman-active modes for (a–d) BTNO and (e-h) BTWN5 ceramics. The solid lines are a guide for the eyes to emphasize the various trends and the vertical shadows are applied to divide the temperature region into various crystal structures.

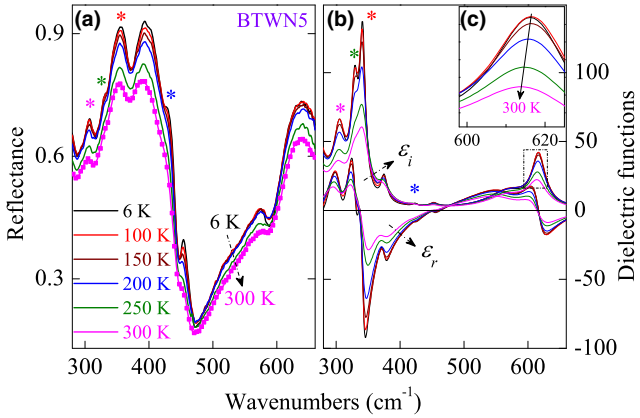

Fig. 5. The temperature-dependent (a) FIR reflectance spectra and (b) corresponding real (ε_r) and imaginary (ε_i) parts of complex dielectric functions of BTWN5. (c) Enlarged real parts in the range 598–625 cm^{-1} and the arrow illustrates the trend of peak position.

vibrations of the Ti/Nb ions, respectively.[24] Moreover, the Raman modes around 820 cm^{-1} relate to the Nb/Ti–O symmetric stretch of TiO_6/NbO_6 octahedra.[25] The various trends of the three modes illustrate that there are two intermediate phase transitions (T_1 ~160 K and T_2 ~600 K for BTNO, and T_1 ~190 K and T_2 ~560 K for BTWN5) in the temperature range 80–800 K. Note that the mode near 590 cm^{-1} has been assigned to a rigid sublattice mode and its trend not obviously changes during phase transitions. The phonon frequency as a function of temperature can be expressed by the perturbation model, which is written as: [31,32] $\omega(T) = \omega_0 + \Delta\omega_e(T) + \Delta\omega_d(T)$, here $\Delta\omega_e(T) = -\omega_0\gamma\int_0^T[\alpha_a(T) + \alpha_b(T) + \alpha_c(T)]\mathrm{d}T$, $\Delta\omega_d(T) = A[1 + 2/(n_1 - 1)] + B[1 + 3/(n - 1) + 3/(n - 1)^2]+$ higher order terms, $n_1 =$ exp $(\hbar\omega_0/2k_BT)$ and $n =$ exp $(\hbar\omega_0/3k_BT)$. The γ is Grüneisen parameter. α_a, α_b, and α_c are the thermal expansion coefficients in the *a*-, *b*-, and *c*-axis, respectively. It should be emphasized that the first term ω_0 represents the harmonic frequency of optical mode, the second one relates to the thermal expansion of the lattice, and the third one corresponds to cubic, quadratic, and higher order anharmonic coupling between phonons. Therefore, the decrease in mode frequency with increasing temperature is mainly due to the thermal expansion. On the contrary, anharmonic multiphonon coupling will predominate when mode frequency increases with increasing temperature.

To confirm the phase transitions of W-doping BTNO ceramics, FIR reflectance spectra of BTWN100*x* ceramics have been recorded in the temperature range 6–300 K. For example, Fig. 5(a) shows the FIR reflectance of BTWN5 ceramic at some typical temperature points. There are two high-reflectance regions of 320–440 and 600–660 cm^{-1}. The low-frequency edge of the reflectance plateau is related to a strongly IR transverse-optical (TO) mode and the high-frequency one is associated with the corresponding longitudinal-optical (LO) one. The spectra are similar to that of another Aurivillius compound $SrBi_2Ta_2O_9$, the space group of which is $A2_1am$ (C_{2v}^{12}).[23] To a certain extent, the crystal structure of BTWN100*x* ceramics at low temperature can be described by the $A2_1am$ space group. It was found that the reflectance intensities decrease upon heating. Moreover, some peaks marked by the symbol asterisk (*) change remarkably with increasing temperature. The positions, intensity, and bandwidth of IR-active phonon modes as well as complex dielectric functions at different temperatures have been extracted by fitting the FIR reflectance spectra using the multi-Lorentzian oscillator functions. The corresponding dielectric functions $\varepsilon_r(\omega)$ and $\varepsilon_i(\omega)$ of BTWN5 ceramic are shown in Fig. 5(b). It suggests that the optical constant values become lower and the bandwidth of modes becomes broadening upon heating. Moreover, the Fig. 5(c) illustrates that the position of the IR mode near 615 cm^{-1} has a shift toward lower wave numbers with increasing temperature due to the unit-cell expansion, leading to elongation of the chemical bonds (i.e., weakening of the interatomic interactions).

Figure 6 shows various temperature-dependent trends of the IR-active modes near 303, 327, 340, and 420 cm^{-1} in BTNO and BTWN5 ceramics. The mode around 303 cm^{-1} of BTNO corresponds to an A_{2u} mode of the tetragonal symmetry, which is associated with the $(Bi_2O_2)^{2+}$ bending

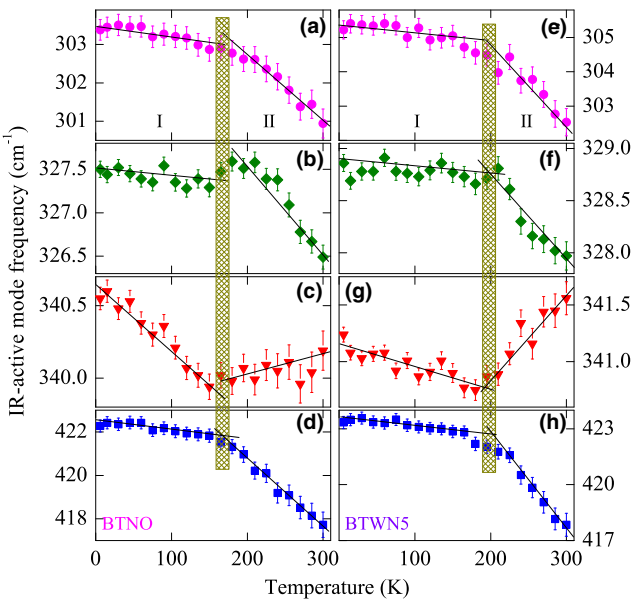

Fig. 6. The various frequency trends of some typical IR-active modes for (a–d) BTNO and (e–h) BTWN5 ceramics. The solid lines are a guide for the eyes to emphasize the various trends and the vertical shadows are applied to divide the temperature region into different crystal structures.

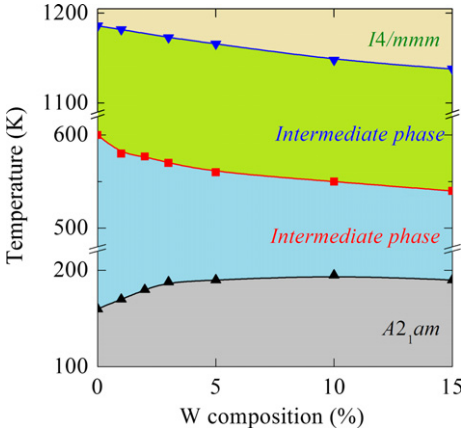

Fig. 7. Phase diagram of BTWN100x ceramics with different W compositions. The phase transition temperatures in this work are marked with the symbol (▲ and ■) and the values marked by the symbol (▼) are our previous work (Ref. [15]).

motions in the direction nearly perpendicular to the layers. Upon heating, its frequency has a shift toward lower wave numbers and the line slopes change at about 160 K for BTNO and 190 K for BTWN5. Furthermore, some other IR-active modes confirm that there is one intermediate phase transition at about 160 K for BTNO [Figs. 6(a)–(d)] and 190 K for BTWN5 [Figs. 6(e-h)]. Obviously, the IR mode near 327 cm^{-1} slightly decreases and then decreases dramatically on heating. On the other hand, the one located around 340 cm^{-1} decreases dramatically and then slightly increases upon heating, which is assigned to the BO_6 stretching.[21,23] In addition, the temperature-dependent behavior of the mode near 420 cm^{-1} is similar to that of the IR mode (303 cm^{-1}), which can be explained by the lattice thermal expansion.

In the case of Aurivillius compounds, phase transitions from high-symmetry to a low-symmetry phase should pass via intermediate phases. It is established experimentally that these transformations involve approximate tiltings and rotations of BO_6 octahedra.[21] The $A2_1am$ symmetry is common for the ferroelectric phase of all simple Aurivillius compounds having perovskite blocks with an even number of octahedra along the stacking direction. In fact, no Landau-type order parameter transforming can explain a direct symmetry break ($I4/mmm \rightarrow A2_1am$) into the ferroelectric phase according to a single irreducible representation (irrep) of $I4/mmm$ (i.e., $A2_1am$ is not an isotropy subgroup of $I4/mmm$).[33] Combining with the results of temperature-dependent Raman and IR spectra, a receivable symmetry breaking in space group, $I4/mmm(139)$ → the first intermediate phase → the second intermediate phase → $A2_1am(36)$, is deduced in BTWN100x ceramics with decreasing temperature. For a further step, the two intermediate phase transitions (T_1 and T_2) between $I4/mmm$ and $A2_1am$ in W-doping BTNO ceramics have been extracted of about 160 and 600 K (BTNO), 170 and 580 K (BTWN1), 180 and 577 K (BTWN2), 188 and 570 K (BTWN3), 190 and 560 K (BTWN5), 195 and 550 K (BTWN10), and 190 and 540 K (BTWN15) based on the comprehensive analysis of temperature-dependent frequencies of the Raman- and IR-active modes. With the present results and earlier studies of BTWN100x ceramics,[15] we have completed a revision of the BTWN100x phase diagram with the two intermediate phases, as shown in Fig. 7. The Curie temperature decreases in the range 1133–1183 K with increasing amount of W^{6+} doping due to the reduction in tilting angle in octahedra.[34]

IV. Conclusions

High-quality single-phase Aurivillius layered ferroelectric $Bi_3Ti_{1-x}W_xNbO_{9+\delta}$ (BTWN100x, $0 \leq x \leq 15\%$) ceramics were prepared by using solid-state reaction sintering. The crystal structure belongs to an orthorhombic phase within the W composition below 15% at room temperature and the W^{6+} ions prefer to occupy the Ti^{4+} site of BTWN100x. Temperature and W-doping effects on Raman- and IR-active modes of BTNO ceramics have been investigated. The variation temperature-dependent trends of optical phonon modes indicate two intermediate phase between $A2_1am$ and $I4/mmm$ phase. Accurately, their crystal structure undergoes paraelectric $I4/mmm$ to two ferroelectric intermediate phases to ferroelectric $A2_1am$ sequence on cooling. Moreover, the dielectric constants become lower with increasing W compositions in the FIR region of 300–650 cm^{-1} due to the compressive stress induced by the W^{6+} substitution of Ti^{4+} ions in BTWN100x ceramics.

Acknowledgments

One of the authors (J. Z. Zhang) is grateful to Dr. Jiajun Zhu, Ping Chang, and Ting Huang for the technical supports. This work was financially supported by Major State Basic Research Development Program of China (grant nos. 2011CB922200 and 2013CB922300), Natural Science Foundation of China (grant nos. 11374097, 61376129, and 61504156), Projects of Science and Technology Commission of Shanghai Municipality (grant nos. 15JC1401600, 14XD1401500, 13JC1402100, 13JC1404200, and 15YF1413900), the Program for Professor of Special Appointment (Eastern Scholar) at Shanghai Institutions of Higher Learning, and Project funded by China Postdoctoral Science Foundation (grant no. 2014M560357).

References

[1]B. H. Park, B. S. Kang, S. D. Bu, T. W. Noh, J. Lee, and W. Jo, "Lanthanum Substituted Bismuth Titanate for Use in Non-Volatile Memories," *Nature*, **401** [6754] 682–4 (1999).
[2]H. N. Lee, D. Hesse, N. Zakharov, and U. Gösele, "Ferroelectric $Bi_{3.25}La_{0.75}Ti_3O_{12}$ Films of Uniform a-Axis Orientation on Silicon Substrates," *Science*, **296** [5575] 2006–9 (2002).
[3]H. X. Yan, H. T. Zhang, R. Ubic, M. J. Reece, J. Liu, et al., "A Lead-Free High-Curie-Point Ferroelectric Ceramic, $CaBi_2Nb_2O_9$," *Adv. Mater.*, **17** [10] 1261–5 (2005).
[4]C. A.-P. De Araujo, J. D. Cuchiaro, L. D. McMillan, M. C. Scott, and J. F. Scott, "Fatigue-Free Ferroelectric Capacitors with Platinum Electrodes," *Nature*, **374** [6523] 627–9 (1995).
[5]J. G. Thompson, A. D. Rae, R. L. Withers, and D. C. Craig, "Revised Structure of Bi_3TiNbO_9," *Acta Cryst*, **47** [2] 174–80 (1991).
[6]Z. Y. Zhou, Y. C. Li, L. H. Yang, X. L. Dong, and H. X. Yan, "Effect of Annealing on Dielectric Behavior and Electrical Conduction of W^{6+} Doped Bi_3TiNbO_9 Ceramics," *Appl. Phys. Lett.*, **90** [21] 212908, 3pp (2007).
[7]Z. G. Yi, Y. X. Li, Z. Y. Wen, S. R. Wang, J. T. Zeng, and Q. R. Yin, "Intergrowth Bi_2WO_6-Bi_3TiNbO_9 Ferroelectrics with High Ionic Conductivity," *Appl. Phys. Lett.*, **86** [19] 192906, 7pp (2005).
[8]X. B. Zhang, P. Z. Gu, and S. B. Desu, "Solid Solution in the $SrBi_2Ta_2O_9$-Bi_3TiNbO_9 System," *Phys. Stat. Sol. (A)*, **160** [1] 35–47 (1997).
[9]H. Irie, M. Miyayama, and T. Kudo, "Structure Dependence of Ferroelectric Properties of Bismuth Layer-Structured Ferroelectric Single Crystals," *J. Appl. Phys.*, **90** [8] 4089–94 (2001).
[10]A. Moure, L. Pardo, C. Alemany, P. Millan, and A. Castro, "Piezoelectric Ceramics Based on Bi_3TiNbO_9 from Mechanochemically Activated Precursors," *J. Eur. Ceram. Soc.*, **21** [10–11] 1399–402 (2001).
[11]K. Shi, L. Peng, M. J. Li, Z. Y. Zhou, K. Jiang, et al., "Structural Distortion, Phonon Behavior and Electronic Transition of Aurivillius Layered Ferroelectric $CaBi_2Nb_{2-x}W_xO_9$ Ceramics," *J. Alloy. Compd.*, **653**, 168–74 (2015).
[12]H. Irie, H. Saito, S. Ohkoshi, and K. Hashimoto, "Enhanced Ferroelectric Properties of Nitrogen-Doped $Bi_4Ti_3O_{12}$ Thin Films," *Adv. Mater.*, **17** [4] 491–4 (2005).
[13]Z.-Y. Zhou, X.-L. Dong, and H.-X. Yan, "Lanthanum Distribution and Dielectric Properties of $Bi_{3-x}La_xTiNbO_9$ Bismuth Layer-Structured Ceramics," *Scripta Mater.*, **55** [9] 791–4 (2006).
[14]E. Buixaderas, M. Berta, L. Kozielski, and I. Gregora, "Raman Spectroscopy of $Pb(Zr_{1-x}Ti_x)O_3$ Graded Ceramics Around the Morphotropic Phase Boundary," *Phase Transitions*, **84** [5–6] 528–41 (2011).
[15]Z. Y. Zhou, X. L. Dong, H. Chen, and H. X. Yan, "Structural and Electrical Properties of W^{6+}-Doped Bi_3TiNbO_9 High-Temperature Piezoceramics," *J. Am. Ceram. Soc.*, **89** [5] 1756–60 (2006).
[16]J. Zhu, X. B. Chen, Z. P. Zhang, and J. C. Shen, "Raman and X-Ray Photoelectron Scattering Study of Lanthanum-Doped Strontium Bismuth Titanate," *Acta Mater.*, **53** [11] 3155–62 (2005).
[17]J. Petzelt and V. Dvorak, "Changes of Infrared and Raman Spectra Induced by Structural Phase Transitions. I. General Considerations," *J. Phys. C: Solid State Phys.*, **9** [8] 1571–86 (1976).
[18]D. Nuzhnyy, S. Kamba, P. Kužel, S. Veljko, V. Bovtun, et al., "Dynamics of the Phase Transitions in Bi-Layered Ferroelectrics with Aurivillius Structure: Dielectric Response in the Terahertz Spectral Range," *Phys. Rev. B*, **74** [13] 134105, 7pp (2006).

[19]Z. Y. Zhou, Y. C. Li, L. H. Yang, X. L. Dong, and Y. L. Wang, "Microstructure and Electrical Properties of Textured Bi-Layered Bi_3TiNbO_9 Piezoceramics," *Ferroelectrics*, **363** [1] 127–33 (2008).

[20]J. Z. Zhang, W.-Y. Tong, J. J. Zhu, J. Y. Xu, Z. H. Duan, et al., "Temperature Dependent Lattice Dynamics and Electronic Transitions of 0.93Pb$(Zn_{1/3}Nb_{2/3})O_3$-0.07$PbTiO_3$ Single Crystals: Experiment and Theory," *Phys. Rev. B*, **91** [8] 085201, 8pp (2015).

[21]Y. E. Kitaev, M. I. Aroyo, and J. M. Perez-Mato, "Site Symmetry Approach to Phase Transitions in Perovskite-Related Ferroelectric Compounds," *Phys. Rev. B*, **75** [6] 064110, 11pp (2007).

[22]J. Z. Zhang, M. J. Han, Y. W. Li, Z. G. Hu, and J. H. Chu, "Enhanced Raman Scattering and Photoluminescence of $Bi_{3.25}La_{0.75}Ti_3O_{12}$ Nanotube Arrays for Optical and Ferroelectric Multifunctional Applications," *Appl. Phys. Lett.*, **101** [8] 081903, 5pp (2012).

[23]M. P. Moret, R. Zallen, R. E. Newnham, P. C. Joshi, and S. B. Desu, "Infrared Activity in the Aurivillius Layered Ferroelectric $SrBi_2Ta_2O_9$," *Phys. Rev. B*, **57** [10] 5715–23 (1998).

[24]P. R. Graves, G. Hua, S. Myhra, and J. G. Thompson, "The Raman Modes of the Aurivillius Phases: Temperature and Polarization Dependence," *J. Solid State Chem.*, **114** [1] 112–22 (1995).

[25]E. Ching-Prado, W. Pérez, P. S. Dobal, R. S. Katiyar, S. Tirumala, and S. B. Desu, "Raman Scattering in the Aurivillius-Layered Ferroelectric $SrBi_2Ta_2O_9$-Bi_3TiNbO_9 Thin Films," *Integr. Ferroelectr.*, **29** [1–2] 33–41 (2000).

[26]K. Wakino, M. Murata, and H. Tamura, "Far Infrared Reflection Spectra of Ba(Zn,Ta)O_3-$BaZrO_3$ Dielectric Resonator Material," *J. Am. Ceram. Soc.*, **69** [1] 34–7 (1986).

[27]E. Buixaderas, D. Nuzhnyy, J. Petzelt, L. Jin, and D. Damjanovic, "Polar Lattice Vibrations and Phase Transition Dynamics in $Pb(Zr_{1-x}Ti_x)O_3$," *Phys. Rev. B*, **84** [18] 184302, 12pp (2011).

[28]F. Cordero, F. Trequattrini, F. Craciun, and C. Galassi, "Octahedral Tilting, Monoclinic Phase and the Phase Diagram of PZT," *J. Phys.: Condens. Matter*, **23** [41] 415901, 10pp (2011).

[29]M. A. Subramanian, D. Li, N. Duan, B. A. Reisner, and A. W. Sleight, "High Dielectric Constant in $ACu_3Ti_4O_{12}$ and $ACu_3Ti_3FeO_{12}$ Phases," *J. Solid State Chem.*, **151** [2] 323–5 (2000).

[30]K. R. Whittle, N. C. Hyatt, and I. M. Reaney, "Phase Transitions in Lanthanum-Doped Strontium Bismuth Tantalate," *Chem. Mater.*, **20** [20] 6427–33 (2008).

[31]Y. L. Zhang, C. X. Harris, P. Wallenmeyer, J. Murowchick, and X. B. Chen, "Asymmetric Lattice Vibrational Characteristics of Rutile TiO_2 as Revealed by Laser Power Dependent Raman Spectroscopy," *J. Phys. Chem. C*, **117** [45] 24015–22 (2013).

[32]S. P. Pavunny, A. Kumar, and R. S. Katiyar, "Raman Spectroscopy and Field Emission Characterization of Delafossite $CuFeO_2$," *J. Appl. Phys.*, **107** [1] 013522, 7pp (2010).

[33]J. M. Perez-Mato, M. Aroyo, A. García, P. Blaha, K. Schwarz, et al., "Competing Structural Instabilities in the Ferroelectric Aurivillius Compound $SrBi_2Ta_2O_9$," *Phys. Rev. B*, **70** [21] 214111, 14pp (2004).

[34]Z. H. Peng, Q. Chen, Y. Chen, D. Q. Xiao, and J. G. Zhu, "Microstructure and Electrical Properties in W/Nb Co-Doped Aurivillius Phase $Bi_4Ti_3O_{12}$ Piezoelectric Ceramics," *Mater. Res. Bull.*, **59**, 125–30 (2014). □